remote sensing

Article

The Feasibility of Remotely Sensed Near-Infrared Reflectance for Soil Moisture Estimation for Agricultural Water Management

Ebrahim Babaeian [1] and Markus Tuller [2,*]

[1] Department of Soil, Water, and Ecosystem Sciences, University of Florida, Gainesville, FL 32611, USA; ebabaeian@ufl.edu
[2] Department of Environmental Science, The University of Arizona, Tucson, AZ 85721, USA
* Correspondence: mtuller@arizona.edu

Abstract: In-depth knowledge about soil moisture dynamics is crucial for irrigation management in precision agriculture. This study evaluates the feasibility of high spatial resolution near-infrared remote sensing with unmanned aerial systems for soil moisture estimation to provide decision support for precision irrigation management. A new trapezoid model based on near-infrared transformed reflectance (NTR) and the normalized difference vegetation index ($NDVI$) is introduced and used for estimation and mapping of root zone soil moisture and plant extractable water. The performance of the proposed approach was evaluated via comparison with ground soil moisture measurements with advanced time domain reflectometry sensors. We found the estimates based on the $NTR - NDVI$ trapezoid model to be highly correlated with the ground soil moisture measurements. We believe that the presented approach shows great potential for farm-scale precision irrigation management but acknowledge that more research for different cropping systems, soil textures, and climatic conditions is needed to make the presented approach viable for the application by crop producers.

Keywords: remote sensing; unmanned aerial systems; near-infrared reflectance; agricultural irrigation management; soil moisture; plant extractable water

Citation: Babaeian, E.; Tuller, M. The Feasibility of Remotely Sensed Near-Infrared Reflectance for Soil Moisture Estimation for Agricultural Water Management. *Remote Sens.* **2023**, *15*, 2736. https://doi.org/10.3390/rs15112736

Academic Editors: Ruxandra Vintila and Frank Veroustrate

Received: 27 April 2023
Revised: 22 May 2023
Accepted: 23 May 2023
Published: 24 May 2023

1. Introduction

Many regions across the world face serious water shortages that have significant ramifications for irrigated agriculture, which are expected to further intensify due to the rapidly growing human population and the changing global climate. Today, many crop producers rely on their experience to manage irrigation, which often leads to excess water being applied out of fear of yield loss. This practice not only depletes precious water resources, but also contributes to water quality deterioration through the release of agrochemicals into surface water and groundwater bodies. The escalating global water crises demands the development and adoption of transformative technologies for precision irrigation management to conserve water resources while reducing the environmental footprint.

Over the last decade, significant efforts have been devoted to the development of remote sensing (RS) techniques for monitoring of soil water status as a measure for plant stress and irrigation demand. Because soil moisture and electromagnetic radiation reflected in the optical, thermal, and microwave domains are strongly correlated, various RS methods have been established for near-surface and root zone soil moisture dynamics characterization and monitoring [1]. Today, several satellites for monitoring near-surface (2–5 cm) soil moisture exist, including NASA's Soil Moisture Active Passive (SMAP) mission [2], the Soil Moisture and Ocean Salinity (SMOS) mission [3] of the European Space Agency (ESA), the ESA/EUMETSAT Advanced Scatterometer (ASCAT) [4], and the ESA Sentinel-1 mission [5].

NASA's Airborne Microwave Observatory of Subcanopy and Subsurface (AirMOSS) P-band radar also shows potential for RS of root zone soil moisture (0–50 cm) [6]. Although microwave satellite-based coarse estimates of soil moisture are valuable and widely applied for large-scale environmental monitoring, their applicability for farm-scale irrigation management is limited due to low spatial resolution, infrequent coverage, clouds, and slow distribution of data to end-users [7]. The same issues exist for near-surface soil moisture retrievals from satellite RS products. This suggests a crucial need for the improvement of RS methods applicable for precision agriculture (PA) irrigation management. A comprehensive review of satellite RS of near-surface and root zone soil moisture is provided in Babaeian et al. [1].

The use of unmanned aerial systems (UAS) is becoming a powerful means for PA applications due to their simple deployment, low operational costs, and their potential for obtaining high spatiotemporal resolution data in the optical and thermal electromagnetic domains, which can be applied to determine farm-scale soil moisture status. Soil moisture and reflectance are strongly correlated in the optical domain (350–2500 nm) [8], where the greatest sensitivity occurs in the short-wave infrared (SWIR) and near-infrared (NIR) bands. Based on the physics of radiative transfer, a trapezoidal space for estimation of soil moisture has been introduced by [9]. This so-called OPtical TRApezoid Model (OPTRAM) is based on constructing a SWIR transformed reflectance (STR)—normalized difference vegetation index ($NDVI$) space, finding the location of image pixels with known STR and $NDVI$, and then translating the values to soil moisture.

Because UAS-mounted high spatial resolution cameras for PA applications only provide visible (Vis) and near-infrared (NIR) data, the objectives of this study are: *(1)* to utilize high spatial resolution UAS Micasense RedEdge camera (Micasense, Inc., Seattle, WA, USA) images to investigate the feasibility of replacing the OPTRAM STR parameter with near-infrared transformed reflectance (NTR) to create a new $NTR - NDVI$ trapezoidal space for soil moisture (SM) estimation; and *(2)* to evaluate the accuracy of the obtained SM estimates based on ground sensor measurements for an irrigated durum wheat field located in Maricopa, Arizona, USA.

2. Materials and Methods

2.1. Estimation of Plant Extractable Water

Rather than relying on absolute soil moisture values for irrigation management, it is common to delineate the plant available water (PAW), which can be derived from the soil water characteristic (SWC), the functional relationship between soil moisture (θ) and the matric potential (h) that exhibits a very distinctive shape for each individual soil texture (Figure 1) [1]. The SWC for a given soil may be measured in the laboratory with standard methods (e.g., Tempe cells for the wet end and chilled mirror dewpoint techniques for the dry end) or with more advanced automated instruments such as the HYPROP system (METER Group, Inc., Pullman, WA, USA) that involves evaporation of water from the surface of an initially saturated soil column while concurrently measuring the change in matric potential and the water mass loss. Another option is to measure the SWC directly in the field via pairing of soil moisture and matric potential sensors and continuously recording the changes of both attributes. This, however, is not practical as irrigated agricultural fields only experience narrow soil moisture and matric potential ranges. To obtain a continuous functional relationship between soil moisture and matric potential, SWC models are commonly parameterized based on the measured matric potential/soil moisture data via nonlinear regression. For this study, we applied the van Genuchten SWC model [10] given as:

$$\theta = \theta_r + (\theta_s - \theta_r)\left[1 + |\alpha h|^n\right]^{\left(\frac{1}{n}-1\right)} \tag{1}$$

where θ, θ_r, and θ_s are the actual, residual, and saturated volumetric water contents ($m^3\ m^{-3}$), respectively, h (m) is the matric potential in length units, and α (m^{-1}) and n (-) are shape parameters of the van Genuchten model.

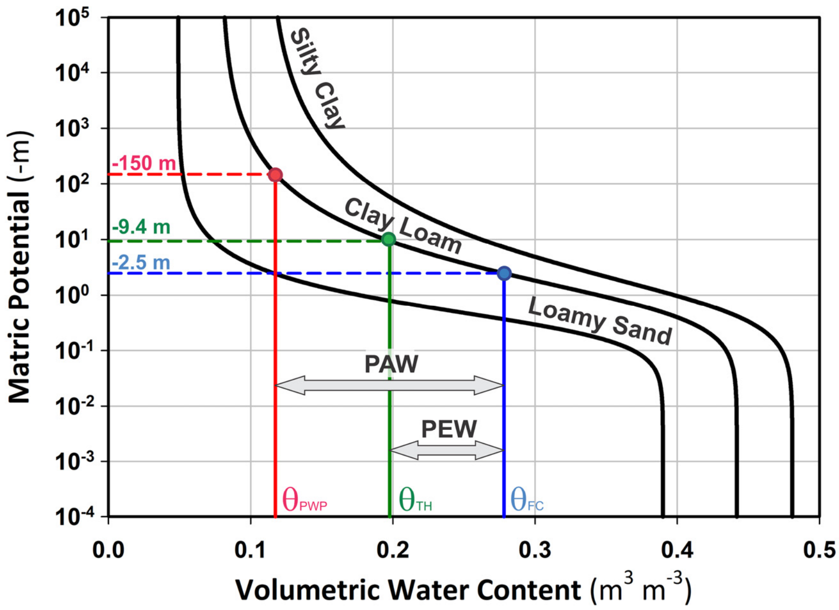

Figure 1. Illustration of the distinct SWC shapes for coarse- (loamy sand), medium- (clay loam), and fine-textured (silty clay) soils and the *PAW* and *PEW* concepts for clay loam.

The *PAW* is commonly defined as the difference between the water content at field capacity (θ_{FC}) and the water content at the permanent wilting point (θ_{PWP}) [11] (Figure 1). The θ_{FC} is defined as the water content after internal redistribution of water within the soil profile due to gravity (free) drainage following an irrigation or precipitation event and for practical purposes is often assumed to coincide with a matric potential of −3.3 m. Because this definition is not entirely correct (i.e., θ_{FC} is dependent on soil texture), we employ the following empirical relationship for θ_{FC} estimation that was developed by [12]:

$$\theta_{FC} = \theta_r + (\theta_s - \theta_r)n^{-0.60(2+\log_{10} K_{SAT})} \tag{2}$$

where K_{SAT} is the saturated hydraulic conductivity of the soil in cm d^{-1}, and n (-) is the shape parameter of the van Genuchten model.

Below the permanent wilting point that is commonly assumed as the water content at −150 m matric potential, water is so tightly bound within the soil matrix that plants are no longer able to recover their turgidity and irreversibly wilt. Again, this is only an approximation, as the permanent wilting point is dependent on plant physiology. Desert plants, for example, can withstand significantly lower matric potentials (i.e., drier conditions) [13], and agricultural crops start wilting prior to approaching the matric potential threshold of −150 m. Because of the latter, for irrigation scheduling, it is advantageous to establish a management allowed depletion (MAD) value [14] and an associated water content threshold (θ_{TH}), which is the portion of the *PAW* allowed to deplete before crops encounter water stress and irrigation is required. This optimal range between θ_{FC} and θ_{TH} is called plant extractable water (*PEW*). Typical values for MAD for shallow-rooted, medium-rooted, and deep-rooted crops have been reported as 0.33, 0.50, and 0.67, respectively [14] with θ_{TH} calculated as:

$$\theta_{TH} = \theta_{FC} - MAD(\theta_{FC} - \theta_{PWP}) \tag{3}$$

Finally, for visualization and mapping, we define the fractional (normalized) plant extractable water (PEW_f) as:

$$PEW_f = \frac{\theta - \theta_{TH}}{\theta_{FC} - \theta_{TH}} \tag{4}$$

When the actual water content θ attains values smaller than θ_{TH}, the PEW_f is negative, which indicates water stress. The PAW and PEW concepts are illustrated in Figure 1 for clay loam texture, with θ_{FC} calculated with Equation (2) and θ_{TH} calculated with Equation (3).

Figure 2 shows the actually measured SWC for the field site that was used to calculate PEW_f. All measurements were performed in quadruplicate with the HYPROP system for wet conditions and the WP4C chilled mirror dewpoint instrument (METER Group, Inc., Pullman, WA, USA) for dry conditions to obtain values for θ_{TH}, θ_{FC}, and θ_{PWP}. A MAD value of 0.5 was applied to determine PEW_f for the durum wheat crop.

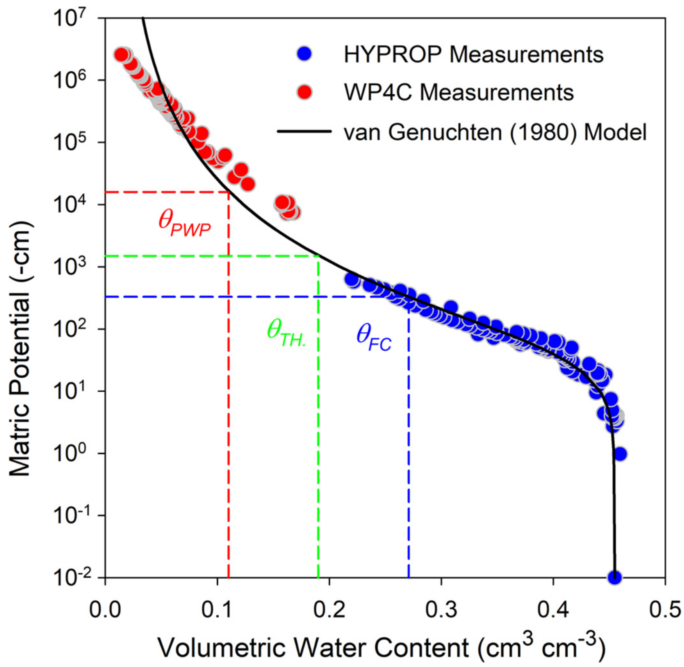

Figure 2. Measured SWC that was used to calculate PEW_f for the field site.

2.2. A New Near-Infrared Trapezoid Model for Soil Moisture Estimation

A nonlinear relationship between relative soil saturation (S_r) and transformed optical surface reflectance (TR) was derived by [8]:

$$S_r = \frac{\theta - \theta_r}{\theta_s - \theta_r} = \frac{\sigma(TR - TR_r)}{TR_s - TR + \sigma(TR - TR_r)} \quad (5)$$

where θ, θ_r, and θ_s are the actual, residual, and saturated volumetric water contents of the soil, respectively, TR_r and TR_s are the transformed optical surface reflectances corresponding to θ_r (i.e., dry soil) and θ_s (i.e., saturated soil), and σ is a shape parameter that ranges from 0 to 1 and represents the concavity of the $TR(\theta)$ relationship. When σ equals 1, the relationship between TR and θ is linear. The relative saturation calculated based on Equation (5) has been validated for bare soils via comprehensive laboratory experiments [8] as well as for vegetated soils based on shortwave infrared satellite observations [9]. It has been determined that σ is affected by the soil texture and the electromagnetic wavelength. The $TR(\theta)$ relationship is nearly linear ($\sigma \sim 1$) for the near-infrared (NIR) frequency domain. Hence, the linear form of Equation (5) may be applied for NIR transformed reflectance (NTR):

$$S_r = \frac{\theta - \theta_r}{\theta_s - \theta_r} = \frac{NTR - NTR_r}{NTR_s - NTR_r} \quad (6)$$

With

$$NTR_r = i_r + s_r NDVI \quad (7)$$

$$NTR_s = i_s + s_s NDVI \tag{8}$$

where i and s are the intercept and slope of the dry and wet edges of the trapezoid in the $NTR - NDVI$ feature space. NTR_r and NTR_s represent the minimum and maximum NIR transformed reflectance values that correspond to θ_r (i.e., dry soil) and θ_s (i.e., saturated soil). Combining Equations (6)–(8) yields relative soil saturation as a function of NTR and $NDVI$ for each image pixel:

$$S_r = \frac{NTR - i_r - s_r NDVI}{i_s - i_r - (s_r - s_s)NDVI} \tag{9}$$

With

$$NTR = \frac{(1 - R_{NIR})^2}{2R_{NIR}} \tag{10}$$

$$NDVI = \frac{R_{NIR} - R_{Red}}{R_{NIR} + R_{Red}} \tag{11}$$

where R_{NIR} and R_{Red} are the surface reflectances corresponding to the NIR and red electromagnetic bands. Assuming that the porosity of the soil is equivalent to θ_s, S_r may be converted to θ via multiplication with θ_s.

Figure 3 depicts a conceptual sketch of the $NTR - NDVI$ trapezoidal feature space with one lower dry edge (D–C line) and two upper wet edges (A–B and B–C lines). Following the first wet edge (A–B), the NTR values increase with increasing $NDVI$ until they reach a maximum that depends on crop variety, density and growth stage, crop canopy and soil moisture status, and soil texture. When $NDVI$ increases beyond point B, NTR decreases due to increasing absorption within the red band and increasing NIR reflectance, forming a second wet edge (B–C line) that meets the dry edge at full crop cover. The dry and wet edges are defined by their specific slopes and intersects, s_r, i_r, s_{s1}, s_{s2}, i_{s1}, and i_{s2}.

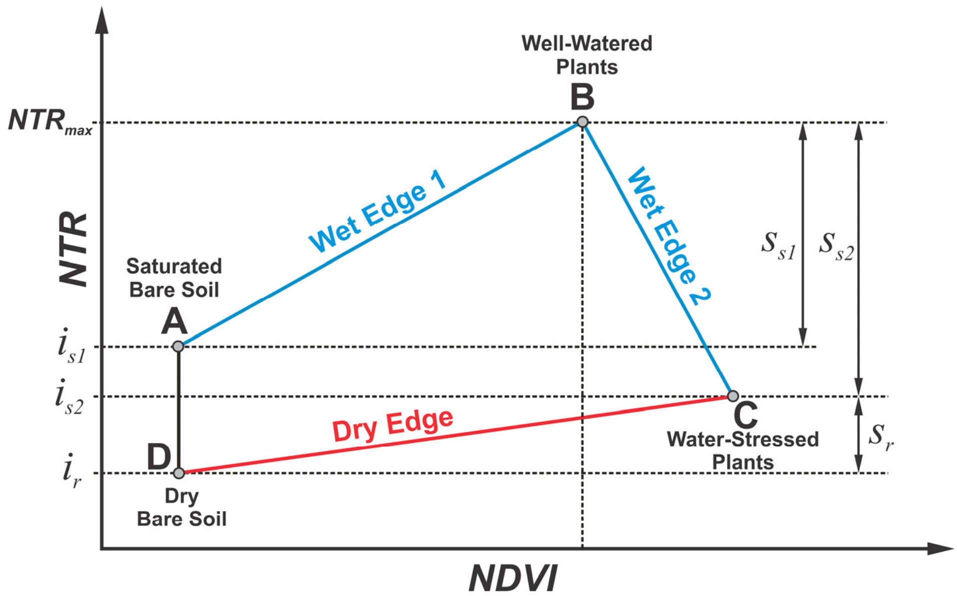

Figure 3. Conceptual sketch of the $NTR - NDVI$ feature space.

2.3. Parameterization of the $NTR - NDVI$ Feature Space

UAS images with high spatial resolution enable capturing soil surface heterogeneities, which adds an additional challenge to data analysis. To accurately derive the $NTR - NDVI$ trapezoids from Micasense RedEdge camera images, pixels that are not associated with soil or vegetation (i.e., shadow pixels) were removed. Shaded pixels exhibit lower reflectance values leading to uncertainties in trapezoid shape and consequently soil moisture estimation. To detect and remove shadow pixels, the supervised maximum likelihood classifier (MLC) image classification method was used. Figure 4 depicts an example of a false color composite image used in the MLC and the three obtained pixel classes including vegetation (wheat), bare soil, and shadows. The advantage of such red and near-infrared based false color composite image is that any small changes in vegetation density and its characteristics (structure, water content, etc.) are highly reflected by these two important spectral bands, leading to a better delineation of soil/vegetation pixels from non-soil/vegetation pixels.

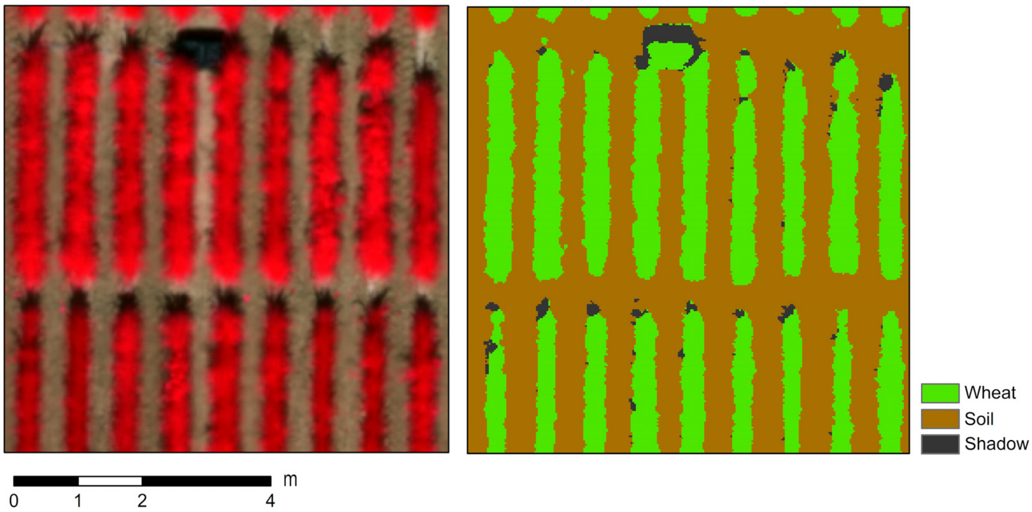

Figure 4. A false color composite image (R-G-B: NIR-Red-Green) (**left**) and the generated maximum likelihood classification map (**right**) 68 days after planting.

We note that the dry and wet edges were manually fitted to the point clouds based on visual inspection. In general, manual fitting may introduce bias and uncertainty, which potentially affects soil moisture estimates. However, according to a sensitivity analysis by [15], who investigated the effects of manual fitting on the accuracy of soil moisture estimation from MODIS satellite images by adding random errors, for the largest uncertainty level (i.e., ±20%), the RMSE only increased by 0.025 cm^3 cm^{-3}. This indicates that manual fitting is a viable option for the presented feasibility study.

2.4. Field Site

For this study, we used high spatial resolution UAS Micasense RedEdge data and soil moisture reference measurements that were collected for durum wheat at a field site in Maricopa, Arizona, USA (Figure 5a). The prevailing soil texture of the field was sandy clay loam with an average organic matter content of 0.5%. The field was instrumented with state-of-the-art time domain reflectometry (TDR) moisture sensors (True TDR-315, Acclima, Inc., Meridian, ID, USA) installed in duplicate at three locations in 2, 10, and 50 cm depths (Figure 5a,b). The TDR-315 sensor houses the entire measurement circuitry, including a microprocessor, within the sensor head and communicates with a datalogger for transfer of processed data via the SDI-12 protocol [16]. The TDR-measured soil moisture data were recorded at 15-min intervals with CR1000 dataloggers (Campbell Scientific, Inc., Logan, UT, USA). After planting the durum wheat on 29 November 2018, the field was initially irrigated with sprinklers for two weeks until seed germination and then with a subsurface drip system installed in 0.15 m depth with irrigation frequency and amount determined based on the TDR sensor moisture measurements and actual crop water demand.

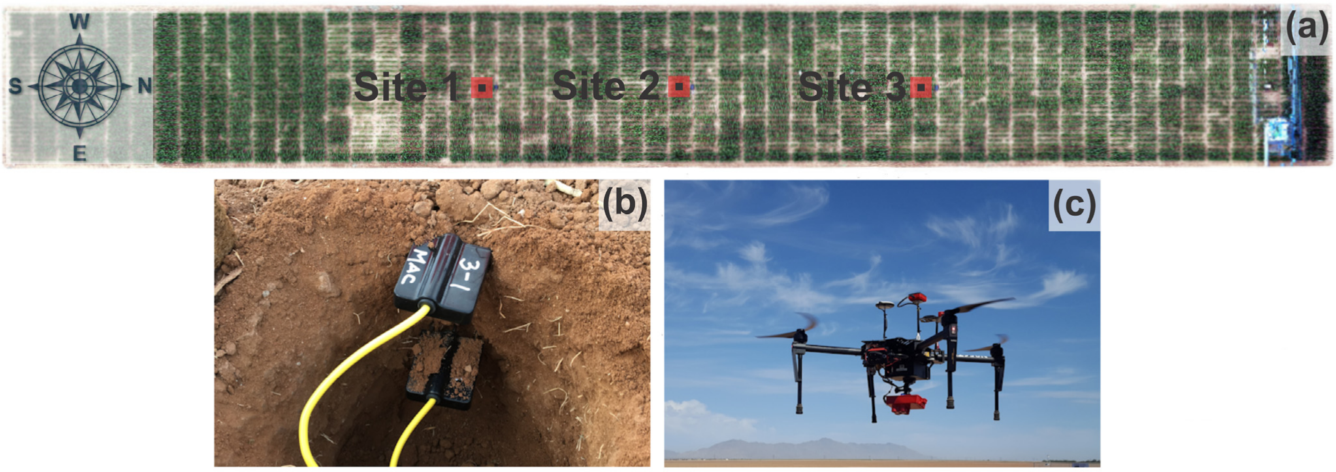

Figure 5. Aerial view of the field site with marked locations (red squares) of the TDR moisture sensor nests (**a**), True TDR-315 sensors installed in duplicate in 2, 10, and 50 cm depths at the three sensor nest locations (**b**), and the DJI Matrice 120 equipped with the Micasense RedEdge camera (**c**).

2.5. UAS Data Collection and Calibration

The deployed UAS platform (Figure 5c) consisted of a DJI Matrice 120 drone (DJI, Shenzhen, China) equipped with a Micasense RedEdge camera (Micasense, Inc., Seattle, WA, USA). The camera specifications and UAS deployment parameters and dates throughout the durum wheat growth season are listed in Table 1. The flight trajectories for the DJI Matrice were designed for the RedEdge camera to collect images with side and forward overlaps of 75% and 80%, respectively [17]. All images were acquired around solar noon local time.

Table 1. Camera specifications and UAS deployment parameters and dates.

Camera	Bands (Wavelength, nm)	Camera Flight Parameters	Deployment Dates
Micasense RedEdge	Blue (475) Green (560) Red (668) Near-Infrared (840) Red Edge (717)	Spatial resolution: 0.026 m Radiometric resolution: 8-bit Field of view: 47.2° Flight height: 43 m Flight speed: 5 m s^{-1}	20 December 2017; 17 January 2018 23 January 2018; 5 February 2018 20 February 2018; 6 March 2018 20 March 2018; 28 March 2018

The data obtained with the Micasense RedEdge camera were calibrated with the Pix4Dmapper software (Pix4D SA, Prilly, Switzerland). The digital numbers of the RedEdge images were converted to reflectance values based on images of manufacturer supplied, 10-cm diameter, reference reflectance panels that were distributed across the field and imaged at the beginning of each flight. The locations of the reference panels were determined with Real Time Kinematic (RTK) precision and used as ground control points (GCPs) to georeference and georectify the orthomosaic maps for each band. Orthomosaic maps were generated from overlapping images taken from different positions and orientations. Using the Pix4Dmapper software, images were first aligned, and sparse 3D point clouds generated. The highly accurate GCPs were then added to the aligned images. The workflow for UAS data processing and soil moisture estimation is shown in Figure 6.

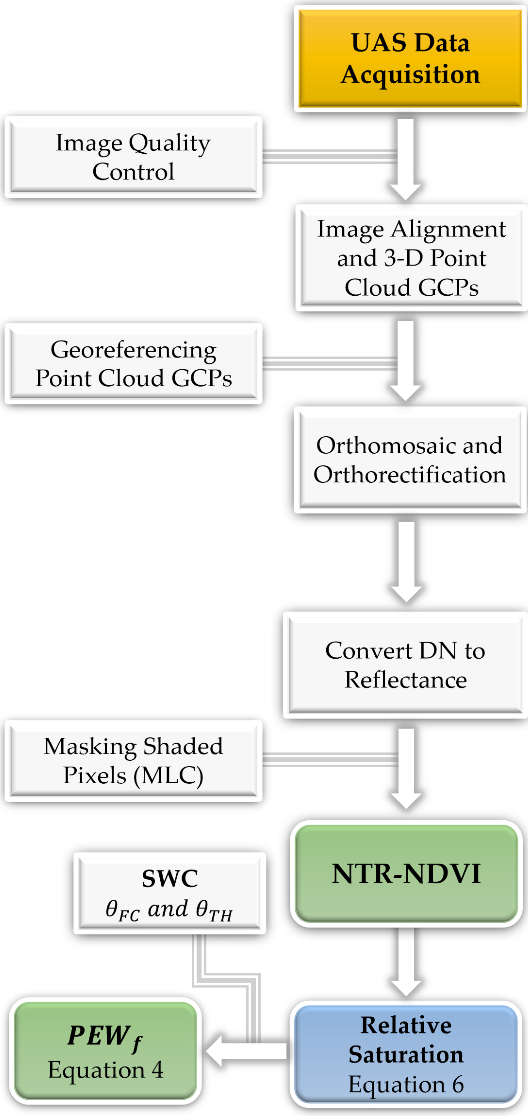

Figure 6. Flowchart illustrating the workflow for UAS data processing and relative saturation estimation.

2.6. Performance Metrics

To evaluate the performance of remotely sensed soil moisture estimates (θ_{RS}) versus ground soil moisture measurements (θ_{TDR}), the bias, the root mean squared error ($RMSE$), and the correlation coefficient (r) were calculated as follows:

$$bias = \frac{1}{N}\sum_{i=1}^{N}(\theta_{RS} - \theta_{TDR})_i \tag{12}$$

$$RMSE = \sqrt{\frac{1}{N}\sum_{i=1}^{N}(\theta_{RS} - \theta_{TDR})_i^2} \tag{13}$$

$$r = \frac{Cov(\theta_{RS}, \theta_{TDR})}{\sqrt{Var(\theta_{RS})Var(\theta_{TDR})}} \tag{14}$$

where N is the number of pairs of estimated and measured soil moisture, and Var and Cov denote variance and covariance of data.

3. Results and Discussion

3.1. Ground Time Domain Reflectometry (TDR) Moisture Sensor Measurements

Figure 7 illustrates irrigation and precipitation events and their effects on soil moisture dynamics within and between plant rows measured with the Acclima TDR sensors for *Site 1* (see Figure 5a,b).

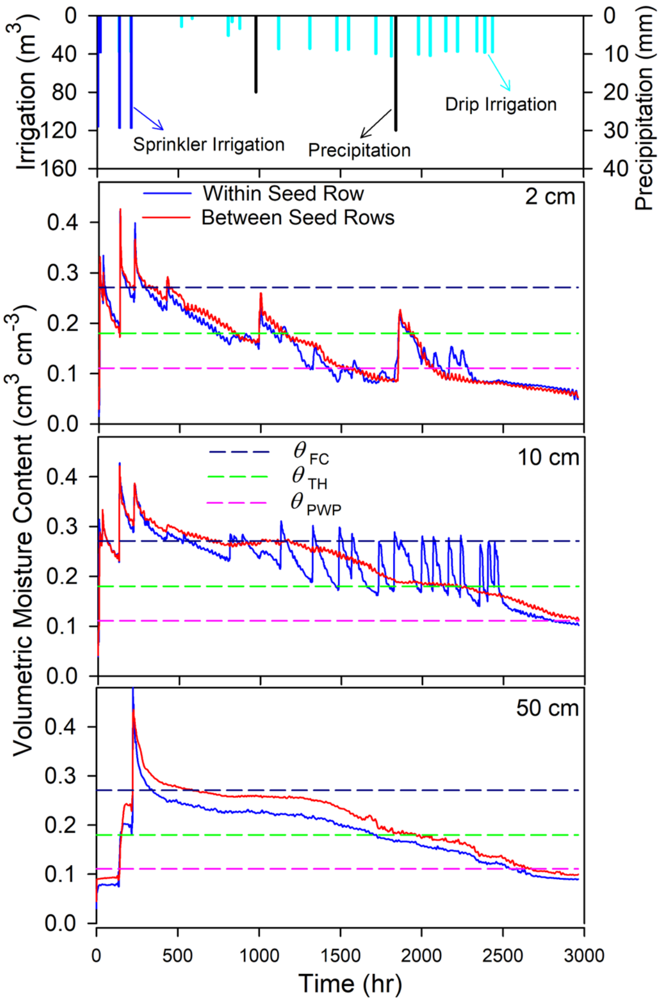

Figure 7. Soil moisture dynamics measured with the Acclima TDR sensors within and between plant rows at *Site 1* plotted together with irrigation and precipitation events. The dashed horizontal black, green, and pink lines mark field capacity (θ_{FC}), threshold soil moisture (θ_{TH}), and the permanent wilting point (θ_{PWP}), respectively.

Good agreement between soil moisture contents measured within and between the plant rows in 2-cm and 50-cm depths can be observed, while there is a large discrepancy between the 10-cm depth measurements, which is attributable to the limited lateral extent of the wetted region because of the installation depth (i.e., 15 cm) of the subsurface drip irrigation system. During the first three weeks (0–500 h), the field was sprinkler irrigated, which led to moisture levels larger than the field capacity (θ_{FC}). After the start of subsurface drip irrigation that was scheduled based on the TDR sensor measurements, optimum moisture content was attained (i.e., $\theta_{TH} \leq \theta \leq \theta_{FC}$ or $0 \leq PEW_f \leq 1$). Because of evaporation of water from the soil surface, the TDR sensor in 2-cm depth shows moisture levels blow θ_{TH}, which indicates that irrigation scheduling based on sensors close to the surface creates a water stress free root zone, but potentially also leads to too frequent irrigation and loss of precious water resources.

3.2. UAS NTR-NDVI Soil Moisture Estimation

The derived $NTR - NDVI$ trapezoids are shown in Figure 8. We can observe that: *(1)* because of high spatial resolution of the RedEdge camera images, a large number of data points is available for assembling the trapezoidal feature space; *(2)* the assembled trapezoids represent the conceptual $NTR - NDVI$ feature space well (see Figure 3) where all data points of NTR vs. $NDVI$ for each acquisition date are within the envelope of the trapezoids; and *(3)* the feature space is confined by two upper wet edges intersecting at the point with maximum NTR (corresponding to point B in Figure 3), and a lower nearly horizontal dry edge intersecting the second wet edges at full vegetation cover (corresponding to point C in Figure 3).

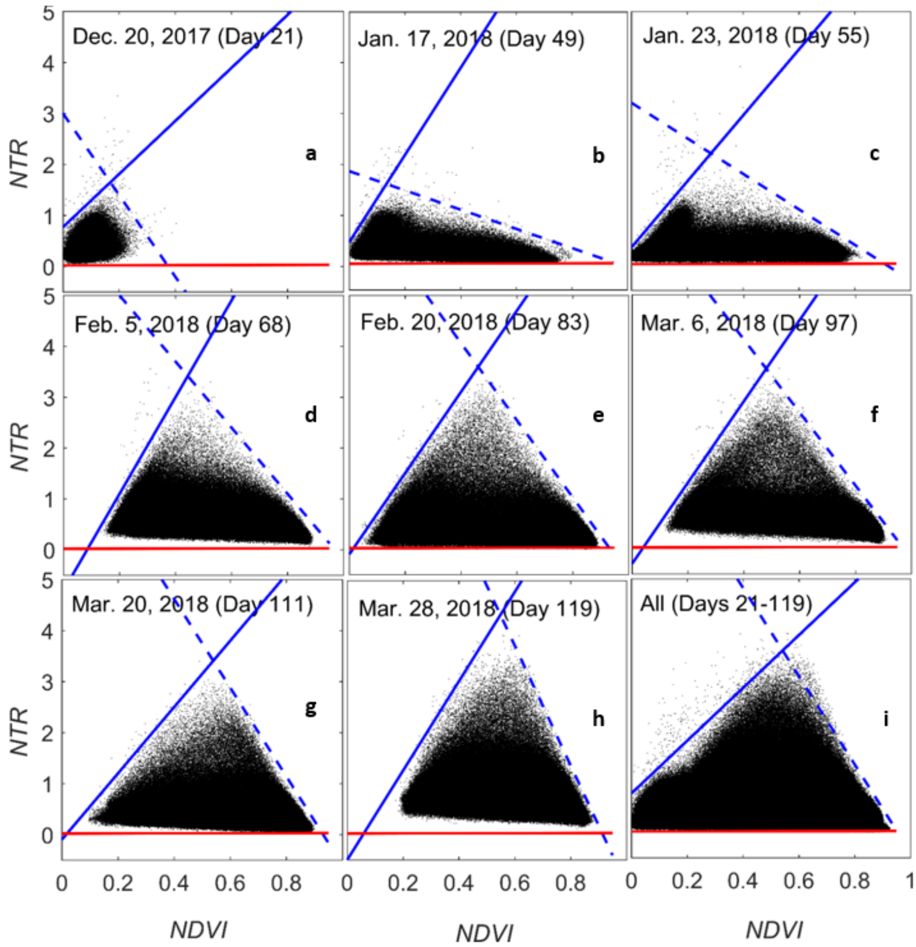

Figure 8. Pixel distribution within the $NTR - NDVI$ space obtained from UAS data for each acquisition date (the days after planting are in brackets). (**a**–**h**) depict individual trapezoids and (**i**) the integrated $NTR - NDVI$ trapezoid. The solid and dashed blue and red lines represent the best fit wet and dry edges.

The plots in Figure 8 show that the NTR and $NDVI$ values are increasing with the evolution of the wheat cover from emergence to maturity with the values ranging from 0 to $\sim$4 for NTR and 0 to $\sim$0.95 for $NDVI$.

The blue and red lines are the manually determined best fit lines for the wet and dry edge data points. Two wet edges and one dry edge are visible. The first wet edge has an upward slope and starts from a small $NDVI$ value and ends with the largest NTR value, which itself is the onset for the second wet edge with downward slope towards the largest $NDVI$ value. Then, we overlayed all eight individual trapezoids (Figure 8a–h) and constructed an integrated trapezoid (Figure 8i) that was ultimately used for estimation of soil moisture. The advantages of such integrated trapezoid are higher computational efficiency and the time independence of the dry and wet edge parameters that provides time stable effective parameters for a given field (crop). The dry and wet edges of the integrated trapezoid were used to parameterize Equations (7) and (8) to estimate relative saturation with Equation (5). The optimized values of the dry and wet edge parameters for the investigated field that can be used for the same field and crop for future soil moisture estimations are: $i_{dry} = 0.02$; $s_{dry} = 0.01$; $i_{wet-1} = 0.77$; $s_{wet-1} = 5.2$; $i_{wet-2} = 8.3$; and $s_{wet-2} = -8.7$.

Figure 9 depicts soil moisture estimated based on the integrated $NTR - NDVI$ trapezoid plotted against soil moisture measured with the Acclima TDR sensors. We see a positive correlation between the estimated and measured soil moisture values, which is strongest for 2-cm depth. The $NTR - NDVI$-derived values overestimate surface soil moisture at 2-cm depth while they underestimate soil moisture in 10-cm and 50-cm depths. This is likely due to the limited penetration depth of optical remote sensing and a scale mismatch between camera pixels and the measurement volume of the Acclima TDR sensors. The relatively high correlation between $NTR - NDVI$ near-surface soil moisture estimates and TDR measurements in deeper depths (i.e., 10 and 50 cm) can be attributed to the connection between surface and root zone soil moisture, which has been previously reported in literature [18–20] and was applied for retrieving root zone soil moisture using data assimilation [21–24].

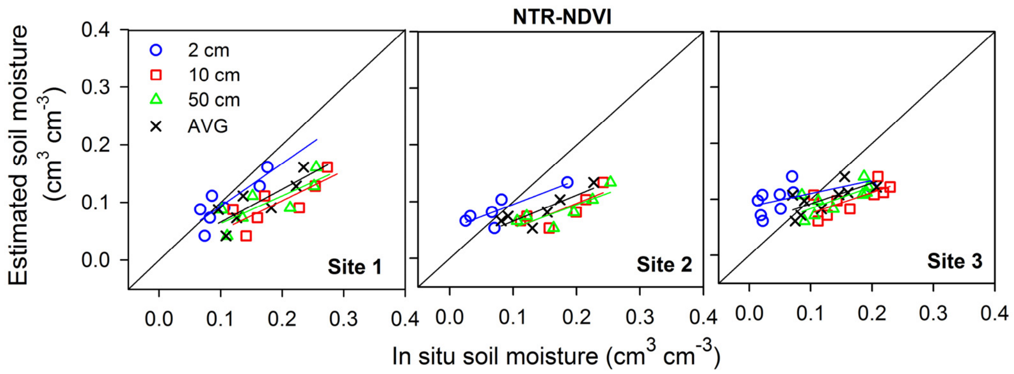

Figure 9. Soil moisture estimated based on the integrated NTR-NDVI trapezoid plotted against soil moisture measured with the Acclima TDR sensors.

The details of the comparison between $NTR - NDVI$ soil moisture estimates and Acclima TDR measurements are summarized in Table 2. Based on the error metrics values listed in Table 2, the $NTR - NDVI$ approach shows reasonable results with correlation coefficients between 0.53 and 0.86, and RMSEs between 0.024 and 0.10 cm^3 cm^{-3}. Overall, the best results were obtained for the near-surface soil layer.

Table 2. Performance of the $NTR - NDVI$ approach for soil moisture estimation.

	NTR−NDVI versus Acclima TDR				
	TDR Sensor Depths	2 cm	10 cm	50 cm	Avg. 2–50 cm
	bias	−0.0088	−0.0937	−0.0753	−0.0593
Site 1	RMSE	0.0237	0.0998	0.0843	0.0665
	r	0.8430	0.7899	0.8040	0.8180
	bias	0.0084	−0.0890	−0.0922	−0.0576
Site 2	RMSE	0.0344	0.0941	0.0985	0.0651
	r	0.8466	0.8199	0.8219	0.8568
	bias	0.0429	−0.0678	−0.0428	−0.0225
Site 3	RMSE	0.0629	0.0755	0.0529	0.0398
	r	0.5310	0.7152	0.7228	0.6949

3.3. Soil Moisture Mapping and Variability

Equation (9) was used to generate soil moisture variability maps for the field site. Previous studies show that because of the connection between near-surface and root zone soil moisture (RZSM), it is feasible to accurately determine RZSM based on near-surface soil moisture estimates [25–27]. However, the strength of this connection depends on many factors such as soil moisture status, climate, and vegetation cover [20]. Figure 10 depicts linear regression functions and correlation coefficients for Acclima TDR sensor measurements in 2-cm depth and the measurements in 10-cm and 50-cm depths, as well as with the average soil moisture from 2–50 cm. The soil moisture in 2-cm depth is highly correlated with the soil moisture in 10-cm depth ($r = 0.81$), 50-cm depth ($r = 0.78$), and the average soil moisture from 2 to 50 cm ($r = 0.91$). Accordingly, the regression derived between soil moisture in 2-cm depth and the 2–50 cm average soil moisture ($y = 0.0645 + 0.85x$) was used to generate an example RZSM map for Site 1 (see Figure 5a) for the 5 February 2018, observation date that is shown in Figure 11. The mapped RZSM values range from 0.08 to 0.46 cm^3 cm^{-3}.

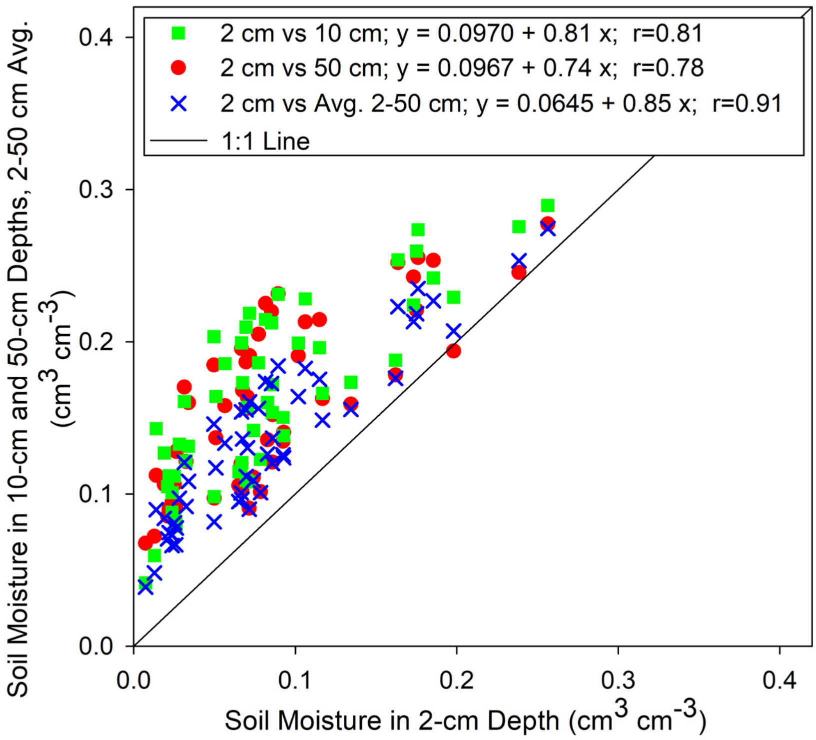

Figure 10. Relationship between Acclima TDR sensor measurements in 2-cm depth and the measurements in 10-cm and 50-cm depths, as well as with the average soil moisture from 2 to 50 cm.

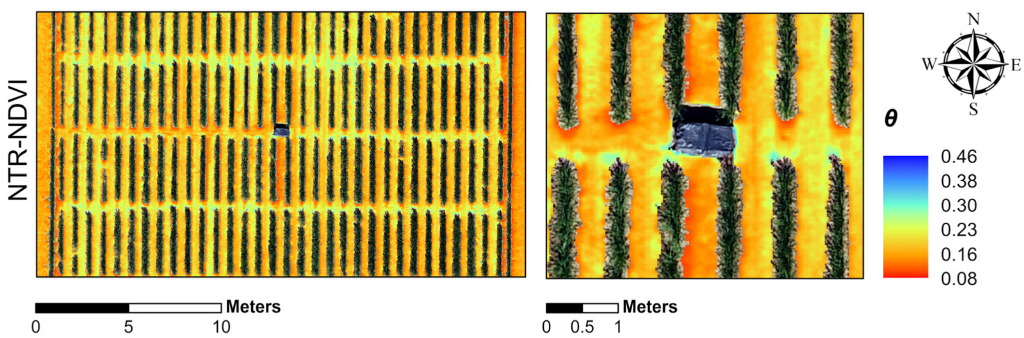

Figure 11. Example high spatial resolution RZSM map for *Site 1* for 5 February 2018.

3.4. Plant Extractable Soil Water Mapping and Variability

Absolute soil moisture values only represent the quantity of water stored in the soil, but do not indicate the ease of water uptake by plant roots. This is why both the amount and availability of water are important for agricultural irrigation management. Within this context, Equation (4) was employed to estimate and map the plant extractable water (PEW_f). PEW_f provides a more reliable measure for water use efficiency or crop water productivity. Figure 12 shows an example PEW_f map for *Site 1* for the 5 February 2018, observation date. The PEW_f values range from -1.4 to 3.4. Negative values (i.e., $\theta_{TH} > \theta$) indicate that there is no available water for uptake by plant roots, while values larger than zero (i.e., $\theta_{TH} < \theta$) imply that water is available for plant root uptake.

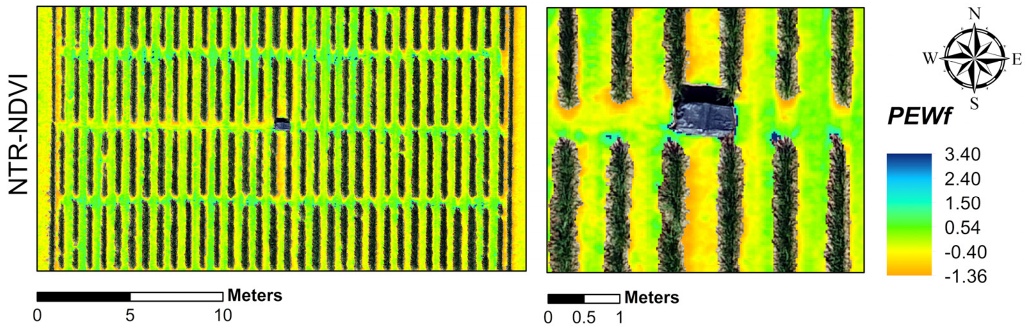

Figure 12. Example high spatial resolution PEW_f map for *Site 1* for 5 February 2018.

A potential application for high spatial resolution RZSM and PEW_f maps is precise irrigation scheduling to optimize irrigation volumes in space and time (e.g., variable rate irrigation with a center pivot system) to meet crop water demand and prevent overirrigation. This contributes to conservation of water resources and reduction of the environmental footprint of farming operations.

4. Summary and Conclusions

The intensifying water crises in arid and semiarid regions of the world demands the development of advanced remote sensing techniques for precise farm level agricultural irrigation management. In this paper, we evaluated the feasibility of using high spatial resolution remotely sensed UAS near-infrared reflectance data in conjunction with ground soil moisture measurements to estimate and map root zone soil moisture (RZSM) and plant extractable water (PEW_f). The tested approach relies on the relationship between near-infrared transformed reflectance (NTR) and the normalized difference vegetation index ($NDVI$), which form a trapezoidal $NTR - NDVI$ feature space. A DJI Matrice 120 UAS equipped with a Micasense RedEdge camera was employed to obtain all data necessary to parameterize the $NTR - NDVI$ feature space for a durum wheat field in Maricopa, AZ, USA.

The performance of the proposed approach was evaluated via comparison with ground soil moisture measurements that were obtained with advanced Acclima time domain reflectometry (TDR) sensors. We found the $NTR - NDVI$ estimates to be highly correlated with the TDR sensor measurements with the best estimation accuracy for the near-surface soil layer. Significant correlations were observed between near-surface and root zone soil moisture measurements, which provided regression functions for the conversion of near-surface soil moisture to RZSM and PEW_f and the creation of associated RZSM and PEW_f maps.

In conclusion, we believe that the presented approach shows great potential for farm-scale precision irrigation management. It could significantly contribute to the conservation of water resources and reduction of the environmental footprint of farming operations. However, we acknowledge that much more research for different cropping systems, soil textures, climatic conditions, and irrigation methods is needed to make the presented approach viable for application by farmers.

Author Contributions: E.B.: Conceptualization, methodology, formal analysis, investigation, data curation, methodology, writing—original draft, and writing—review and editing. M.T.: Conceptualization, methodology, investigation, writing—original draft, and writing—review and editing, supervision, project administration, and funding acquisition. All authors have read and agreed to the published version of the manuscript.

Funding: This research was partially funded by the United States Department of Agriculture (USDA) National Institute of Food and Agriculture (NIFA) under grant #2020-67019-31028, and by the USDA NIFA Hatch/Multi-State project # ARZT-1370600-R21-189.

Data Availability Statement: All data analyzed or generated in the course of the presented study are available from the authors upon request.

Acknowledgments: The authors gratefully acknowledge the support of Richard Ward, who provided the UAS data, and the assistance of Maria Newcomb, Juan Gonzalez Cena, and Scott White with field work and ground soil moisture data collection.

Conflicts of Interest: The authors declare no conflict of interest.

References

1. Babaeian, E.; Sadeghi, M.; Jones, S.B.; Montzka, C.; Vereecken, H.; Tuller, M. Ground, Proximal, and Satellite Remote Sensing of Soil Moisture. *Rev. Geophys.* **2019**, *57*, 530–616. [CrossRef]
2. Entekhabi, D.; Njoku, E.G.; O'Neill, P.E.; Kellogg, K.H.; Crow, W.T.; Edelstein, W.N.; Entin, J.K.; Goodman, S.D.; Jackson, T.J.; Johnson, J.; et al. The Soil Moisture Active Passive (SMAP) Mission. *Proc. IEEE* **2010**, *98*, 704–716. [CrossRef]
3. Kerr, Y.H.; Waldteufel, P.; Wigneron, J.-P.; Martinuzzi, J.-M.; Font, J.; Berger, M. Soil Moisture Retrieval from Space: The Soil Moisture and Ocean Salinity (SMOS) Mission. *IEEE Trans. Geosci. Remote Sens.* **2001**, *39*, 1729–1735. [CrossRef]
4. Bartalis, Z.; Wagner, W.; Naeimi, V.; Hasenauer, S.; Scipal, K.; Bonekamp, H.; Figa, J.; Anderson, C. Initial soil moisture retrievals from the METOP-A Advanced Scatterometer (ASCAT). *Geophys. Res. Lett.* **2007**, *34*, L20401. [CrossRef]
5. Paloscia, S.; Pettinato, S.; Santi, E.; Notarnicola, C.; Pasolli, L.; Reppucci, A. Soil moisture mapping using Sentinel-1 images: Algorithm and preliminary validation. *Remote Sens. Environ.* **2013**, *134*, 234–248. [CrossRef]
6. Sadeghi, M.; Tabatabaeenejad, A.; Tuller, M.; Moghaddam, M.; Jones, S.B. Advancing NASA's AirMOSS P-Band Radar Root Zone Soil Moisture Retrieval Algorithm via Incorporation of Richards' Equation. *Remote Sens.* **2017**, *9*, 17. [CrossRef]
7. Mulla, D.J. Twenty five years of remote sensing in precision agriculture: Key advances and remaining knowledge gaps. *Biosyst. Eng.* **2013**, *114*, 358–371. [CrossRef]
8. Sadeghi, M.; Jones, S.B.; Philpot, W.D. A linear physically-based model for remote sensing of soil moisture using short wave infrared bands. *Remote Sens. Environ.* **2015**, *164*, 66–76. [CrossRef]
9. Sadeghi, M.; Babaeian, E.; Tuller, M.; Jones, S.B. The optical trapezoid model: A novel approach to remote sensing of soil moisture applied to Sentinel-2 and Landsat-8 observations. *Remote Sens. Environ.* **2017**, *198*, 52–68. [CrossRef]
10. van Genuchten, M.T. A closed-form equation for predicting the hydraulic conductivity of unsaturated soils. *Soil Sci. Soc. Am. J.* **1980**, *44*, 892–898. [CrossRef]
11. Kirkham, M.B. *Principles of Soil and Plant Water Relations*, 2nd ed.; Academic Press: Cambridge, MA, USA, 2014; pp. 153–170.
12. Twarakavi, N.K.C.; Sakai, M.; Šimůnek, J. An objective analysis of the dynamic nature of field capacity. *Water Resour. Res.* **2009**, *45*, W10410. [CrossRef]
13. Kappen, L.; Lange, O.L.; Schulze, E.-D.; Evenari, M.; Buschbom, U. Extreme water stress and photosynthetic activity of the desert plant *Artemisia herba-alba* asso. *Oecologia* **1972**, *10*, 177–182. [CrossRef] [PubMed]
14. Cuenca, R.H. *Irrigation System Design: An Engineering Approach*; Prentice Hall: Englewood, NJ, USA, 1989; pp. 176–188.
15. Babaeian, E.; Sadeghi, M.; Franz, T.E.; Jones, S.B.; Tuller, M. Mapping soil moisture with the OPtical TRApezoid Model (OPTRAM) based on long-term MODIS observations. *Remote Sens. Environ.* **2018**, *211*, 425–440. [CrossRef]
16. Schwartz, R.C.; Evett, S.R.; Anderson, S.K.; Anderson, D.J. Evaluation of a Direct-Coupled Time-Domain Reflectometry for Determination of Soil Water Content and Bulk Electrical Conductivity. *Vadose Zone J.* **2016**, *15*, 1–8. [CrossRef]
17. Condorelli, G.E.; Maccaferri, M.; Newcomb, M.; Andrade-Sanchez, P.; White, J.W.; French, A.N.; Sciara, G.; Ward, R.; Tuberosa, R. Comparative Aerial and Ground Based High Throughput Phenotyping for the Genetic Dissection of NDVI as a Proxy for Drought Adaptive Traits in Durum Wheat. *Front. Plant Sci.* **2018**, *9*, 893. [CrossRef]
18. Wu, W.; Dickinson, R.E. Time Scales of Layered Soil Moisture Memory in the Context of Land-Atmosphere Interaction. *J. Clim.* **2004**, *17*, 2752–2764. [CrossRef]
19. Mahmood, R.; Hubbard, K.G. Relationship between soil moisture of near surface and multiple depths of the root zone under heterogeneous land uses and varying hydroclimatic conditions. *Hydrol. Process.* **2007**, *21*, 3449–3462. [CrossRef]

20. Ford, T.W.; Harris, E.; Quiring, S.M. Estimating root zone soil moisture using near-surface observations from SMOS. *Hydrol. Earth Syst. Sci.* **2014**, *18*, 139–154. [CrossRef]
21. Das, N.N.; Mohanty, B.P.; Cosh, M.H.; Jackson, T.J. Modeling and assimilation of root zone soil moisture using remote sensing observations in Walnut Gulch watershed during SMEX04. *Remote Sens. Environ.* **2008**, *112*, 415–429. [CrossRef]
22. Draper, C.S.; Reichle, R.H.; De Lannoy, G.J.M.; Liu, Q. Assimilation of passive and active microwave soil moisture retrievals. *Geophys. Res. Lett.* **2012**, *39*, L04401. [CrossRef]
23. Dumedah, G.; Walker, J.P.; Merlin, O. Root-zone soil moisture estimation from assimilation of downscaled Soil Moisture and Ocean Salinity data. *Adv. Water Resour.* **2015**, *84*, 14–22. [CrossRef]
24. Montzka, C.; Moradkhani, H.; Weihermüller, L.; Hendricks Franssen, H.-J.; Canty, M.; Vereecken, H. Hydraulic parameter estimation by remotely-sensed top soil moisture observations with the particle filter. *J. Hydrol.* **2011**, *399*, 410–421. [CrossRef]
25. Wigneron, J.-P.; Olioso, A.; Calvet, J.-C.; Bertuzzi, P. Estimating root zone soil moisture from surface soil moisture data and soil-vegetation-atmosphere transfer modeling. *Water Resour. Res.* **1999**, *35*, 3735–3745. [CrossRef]
26. Manfreda, S.; Brocca, L.; Moramarco, T.; Melone, F.; Sheffield, J. A physically based approach for the estimation of root-zone soil moisture from surface measurements. *Hydrol. Earth Syst. Sci.* **2014**, *18*, 1199–1212. [CrossRef]
27. Baldwin, D.; Manfreda, S.; Keller, K.; Smithwick, E.A.H. Predicting root zone soil moisture with soil properties and satellite near-surface moisture data across the conterminous United States. *J. Hydrol.* **2017**, *546*, 393–404. [CrossRef]